


Article

Effect of Laser Remelting Power on Immersion Corrosion of Amorphous Al–Ti–Ni Coatings

Haixiang Chen ¹ and Dejun Kong ^{1,2,*} 

¹ College of Mechanical Engineering, Changzhou University, Changzhou 213164, China; chenhaixiang78@163.com

² Changzhou Key Laboratory of Advanced Mould Manufacturing Technology, Changzhou University, Changzhou 213164, China

* Correspondence: djkong@cczu.edu.cn; Tel.: +86-519-8116-9810; Fax: +86-519-8116-9812

Received: 19 November 2017; Accepted: 22 January 2018; Published: 25 January 2018

Abstract: An arc-sprayed amorphous Al–Ti–Ni coating on S355 structural steel was processed by laser remelting (LR) at powers of 600, 800, and 1000 W. The surface-cross-sectional morphologies, chemical element distributions, and phase compositions of the as-obtained Al–Ti–Ni coatings were analyzed using a scanning electron microscope (SEM), energy-dispersive spectrometer (EDS), and X-ray diffractometer (XRD), respectively. The immersion corrosion tests of Al–Ti–Ni coatings in 3.5% NaCl solution for 720 h were performed to investigate the effects of LR power on their immersion corrosion behaviors. The test results show that the amorphous Al–Ti–Ni coatings form good metallurgical bonding with the substrate after LR. The AlNi, Al₃Ti, Al₃Ni₂, Ti₃O₅, and Al₂O₃ amorphous phases are detected in the Al–Ti–Ni coatings after LR. The corrosion potentials of Al–Ti–Ni coatings after LR show a positive shift relative to that of S355 steel, implying that the corrosion resistance of Al–Ti–Ni coatings was superior to that of S355 steel. A dense protective Al₂O₃ film is formed on the Al–Ti–Ni coating surface at an LR power of 1000 W, at which power the highest corrosion potential of –0.233 V is observed. The corrosion mechanisms of Al–Ti–Ni coating at the LR power of 1000 W are uniform corrosion and pitting corrosion, while those of Al–Ti–Ni coatings at the LR powers of 600 and 800 W are localized corrosion and pitting corrosion. The corrosion resistance of Al–Ti–Ni coating with the LR power of 1000 W is better than those at the LR powers of 600 and 800 W, effectively improving the corrosion resistance of S355 steel.

Keywords: arc spraying; laser remelting (LR); Al–Ti–Ni coating; immersion corrosion; electrochemical corrosion

1. Introduction

Offshore platforms are usually made of metallic materials, such as S355 low-alloy structural steel [1]; chloride ions present in the marine environment can be a cause of corrosion for offshore platforms in seawater [2,3]. Immersion corrosion is one of the most serious failures in the marine environment [4]. In the absence of effective corrosion protection measures, the offshore platform will suffer from severe corrosion in a few years, and the corrosion loss will surpass the damage caused by other natural disasters. During the service life of S355 steel on offshore platforms, it is subjected to various kinds of natural loads for long periods of time [5,6]. The corrosion degradation of S355 steel can lead to severe safety issues and even catastrophic events, causing significant economic losses; 25%–45% of corrosion losses can be prevented by adopting effective corrosion protection measures. Therefore, the development of anti-corrosion materials and technologies for offshore platforms is of great economic value.

As a new type of alloy material, amorphous alloy possesses unique characteristics such as atom long range disorder and crystal defects. The amorphous alloy has no interface, its structural

units are in the form of polyhedral clusters of atoms, and some clusters place in groups to form supercluster structures [7], which have to be subjected to a very large external force to make them deform. Furthermore, the bonding between amorphous atoms is much stronger than the crystal due to the lack of a structural defect; therefore, the amorphous alloy improves its strength and hardness. The amorphous alloy has higher corrosion-resistance than the crystalline metal due to the absence of structural defects such as grain boundaries and dislocations, in which the corrosion often occurs preferentially. At the same time, the high activity of the amorphous alloy can also rapidly form a passive film on the surface [8]. Due to the homogeneity of its structure and composition, the formation of a highly corrosion-resistant film is guaranteed. Therefore, amorphous alloys have attracted extensive research attention worldwide. An amorphous alloy is usually controlled via rapid cooling of liquid metal [9] to prevent nucleation and growth of crystals. Al-based amorphous alloys have shown great potential in recent years owing to their low density, high strength, and excellent corrosion resistance [10]. Unfortunately, their glass-forming ability is hampered by conventional fabrication methods [11]. Most Al-based metallic glasses are marginal glass formers and are therefore required to have higher critical cooling rates (10^5 – 10^6 K/s) [12]. Therefore, the rapid solidification techniques are required to fabricate Al-based metallic glasses.

At present, application of a thermal-sprayed Al coating is one of the most economical and effective techniques for improving the corrosion resistance of S355 steel [10,13]. Arc spraying is the primary method for fabrication of Al coatings given its advantages of low cost, high production efficiency, and ease of control of components. The typical thickness of the arc-sprayed Al coating is 200 μm [14]. However, an arc-sprayed Al coating has a typical layered structure. Fully melted particles having high temperatures and high velocities usually cause significant droplet deformation on the substrate surface, which results in the formation of thin layers or lamella that adhere to the substrate surface; subsequently, rapidly solidified layers are continuously formed from a continuous stream of fully melted particles. Sprayed particles include fully melted, semi-melted, and unmelted particles. Because of the uneven and irregular shape of arc-sprayed Al particles when arriving at the Al coating surface, they lead to the poor continuity of the layered structure and incomplete overlapping among the Al particles and, as a result, voids are formed between the layered structures. When the semi-melted and unmelted particles reach the substrate, they cannot fill the voids and consequently form pores, which eventually expand and connect to the cracks [15,16]. The seawater can easily penetrate into the substrate through the defects, which reduce its corrosion resistance [10] and limit its application scope and service life.

Laser remelting (LR) has been used in studies to achieve rapid solidification. The short-duration and high-density laser leads to high-speed heating and melting, which is inevitably followed by a rapid solidification process. The high cooling rate of the rapid solidification process (10^5 – 10^8 K/s) naturally achieved by LR is advantageous for the formation of amorphous alloys [17–19], which when used as coatings improve the corrosion resistance of metallic material. Moreover, LR can eliminate pores, destroy the layered structure, and remelt the entire thickness of the arc-sprayed coating; this results in the formation of a metallurgical bonding between the Al coating and the substrate and provides an extremely low rate of dilution of the coating, which is, in turn, beneficial for improving the bonding strength and corrosion resistance of the coating [20–22]. Therefore, LR is one of the most effective ways to improve the corrosion resistance of arc-sprayed Al coatings. The corrosion resistance of metallic glasses is influenced by the element composition, the corrosion resistance mechanism of metallic glass composites need further research [23,24]. Ti and Ni particles incorporated into a coating can offer optimized protection and improve the microstructure of composite coating. Desirable evolution of the microstructure results in enhancing the anti-wear properties and anti-corrosion properties and high hardness of composite coating [25].

Tan et al. [26] fabricated an Al-based amorphous–nanocrystalline composite coating by laser cladding of AZ80 magnesium alloy under water cooling. Wang et al. [27] studied the effects of LR and annealing on the microstructure, mechanical properties, and corrosion resistance of

Fe-based amorphous–crystalline composite coatings. Li et al. [28] investigated the influence of remelting scanning speed on the amorphous forming ability of Ni-based alloy fabricated by laser cladding and LR. Wang et al. [29] analyzed the microstructure and corrosion resistance of Fe-based amorphous–nanocrystalline coating fabricated by laser cladding. Previous works [26,29] were performed on the use of LR; however, the effects of parameters of the LR process on the corrosion resistance of amorphous Al coating have seldom been reported. LR process parameters mainly include the laser output power, scanning speed, shape and size of the beam spot. The quality of laser-remelted Al coating is influenced by the above parameters; among these process parameters, the laser output power (i.e., LR power) is an important parameter affecting the quality of Al coating. The increasing laser beam energy with increasing output power is beneficial to the melting of Al coating. However, the surface temperature overheats and burns the Al coating with an increase in the LR power. Conversely, when the LR power is too low, the Al coating cannot be remelted completely. Therefore, it is crucial to investigate the influence of LR power on the microstructures and corrosion resistance of Al coating. Thus, in this study, an arc-sprayed amorphous Al–Ti–Ni coating on S355 steel was processed by LR at the laser powers of 600, 800, and 1000 W. The surface-cross-sectional morphologies, element distributions, and phases of the obtained coatings were analyzed using a scanning electron microscope (SEM), energy-dispersive spectrometer (EDS), and X-ray diffractometer (XRD), respectively. Further, their immersion corrosion behaviors in 3.5% NaCl solution for 720 h were also investigated. The effects of LR power on the microstructures, immersion corrosion, and electrochemical corrosion of amorphous Al–Ti–Ni coatings were investigated, which provided a theoretical basis for the application of amorphous Al–Ti–Ni coatings on offshore platforms.

2. Experimental

European standard S355 structural steel was used as the base material; its composition is listed in Table 1.

Table 1. Composition of S355 structural steel (wt %).

C	Si	Mn	P	Cr	S	Ni	Mo	Zr	Fe
0.17	0.55	0.94	0.035	0.065	0.035	0.065	0.30	0.15	Bal.

Before the arc-spraying test, the substrate surface was abraded with #400 sandpaper. The sample was subjected to the following pre-treatment before arc spraying: mechanical polishing → chemical degreasing → roughening treatment → workpiece preheating. Then, the arc-spraying process was performed as follows: arc spraying → cooling → surface cleaning. The arc-spraying material was composed of Al-wire-cored Ti and Ni powders with a diameter of 2 mm, i.e., Al-packed Ti and Ni powders; the cross-section of the material is shown in Figure 1.

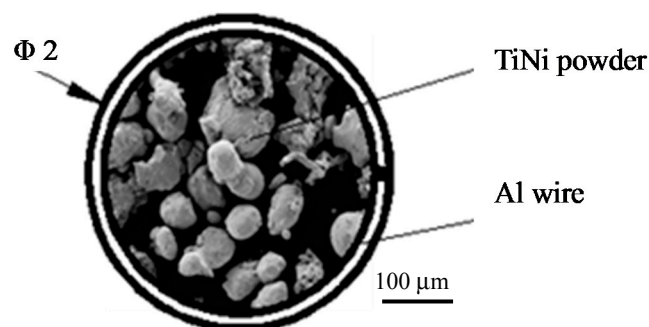


Figure 1. Cross-section of Al-wire-cored Ti and Ni powders.

After arc spraying twice, the thickness of the Al coating was $\sim 600 \mu\text{m}$. The morphologies of Ti–Ni powders were analyzed using SEM (JSM-6360LA, NEC Electronics Corporation, Tokyo, Japan), and its phases were analyzed using PC XRD (D/MAX2500, Rigaku Corporation, Tokyo, Japan). The specifications of the arc-spraying process are listed in Table 2.

The LR process was conducted using a ZKSX-2008 (Jiangsu Zhongke Sixiang Laser Technology Co., Ltd., Danyang, China) fiber-coupled laser spraying system at powers of 600, 800, and 1000 W. Argon gas was employed as protective gas during the LR process. The technical parameters of LR process were as follows: the spot diameter was 4 mm, the overlap ratio was 50%, and the argon gas speed was 15 L/min. After the LR process, the surface-cross sectional morphologies and chemical elements of Al–Ti–Ni coating were analyzed using field-emission SEM (FE-SEM, SUPRA55, Zeiss Corporation, Oberkochen, Germany) and its configured EDS, and their phases were analyzed using PC XRD. The immersion corrosion test was performed in a YQW-250 (Wuhan Test Equipment Co., Ltd., Wuhan, China) immersion corrosion test chamber in accordance with the Chinese standard GB 6458-86 (NSS) [30]. The technical parameters of the immersion corrosion test were as follows: the corrosion solution was $3.5\% \pm 0.5\%$ NaCl, pH was 6.5–7.2, temperature was $26 \pm 7^\circ\text{C}$, and immersion time was 720 h. The reason for selecting 3.5% NaCl was that the concentration of seawater was approximately 3.5%, which was used to simulate this seawater condition. The level of dissolved oxygen (DO) in the 3.5% NaCl testing solution was $\sim 9 \text{ mg/L}$. The immersion time of 720 h was selected on the basis of a measurement by a neutral salt spray test according to the Chinese standard GB/T10125-1997. The morphologies, chemical element distributions, and phases of Al–Ti–Ni coatings after immersion corrosion were analyzed using an FE-SEM, EDS, and XRD, respectively. The electrochemical performance tests were conducted on a CHI660E (Shanghai Chen Hua Instrument Co., Ltd., Shanghai, China) type electrochemical workstation, and the sample size used in the test was $15 \text{ mm} \times 15 \text{ mm} \times 5 \text{ mm}$. The other surfaces were coated and soaked for 5–10 min before the electrochemical test, and the corrosive medium was 3.5% NaCl solution. The potentiodynamic test was adopted, the applied potentials were at the range of -1 to -0.5 V against the saturated calomel electrode (SCE) at the scanning rate of 0.001 V/s , its sensitivity was $1 \times 10^{-0.002}$, and the quiet time of 2 s. A mercury-type KCl saturated calomel electrode was used as the reference electrode, its test time was 1500 s.

Table 2. Specifications of arc-sprayed Al–Ti–Ni coating.

Parameter	Value
Diameter of Al wire/mm	2
Spraying voltage/V	30–32
Spraying current/A	160
Spraying distance/mm	150
Spraying angle/ $^\circ$	80
Spraying pressure/MPa	0.6
Overlap ratio	35%

3. Analysis and Discussion

3.1. Morphologies and EDS Analysis of Ti–Ni Powder

The morphology of Ti–Ni powder is shown in Figure 2a. Particle A was Ni; these particles were flat-ball-like in shape and their surface was compact to flat. Particle B was Ti; these particles were highly irregular in shape and their surface was loose, uneven, and rough. The image mapping result of Ti–Ni powders is shown in Figure 2b. The Ti and Ni particles were the components of Ti–Ni powder, while the C and O were impurity elements. The EDS analysis results of Ni and Ti particles are shown in Figure 2c,d. The Ti and Ni particles, in turn, were composed primarily of Ti and Ni elements, respectively. The C and O elements present in the powders were impurity elements. The Pt present on the surface of the sample resulted from the sputtering process performed to enhance the sample electrical conductivity.

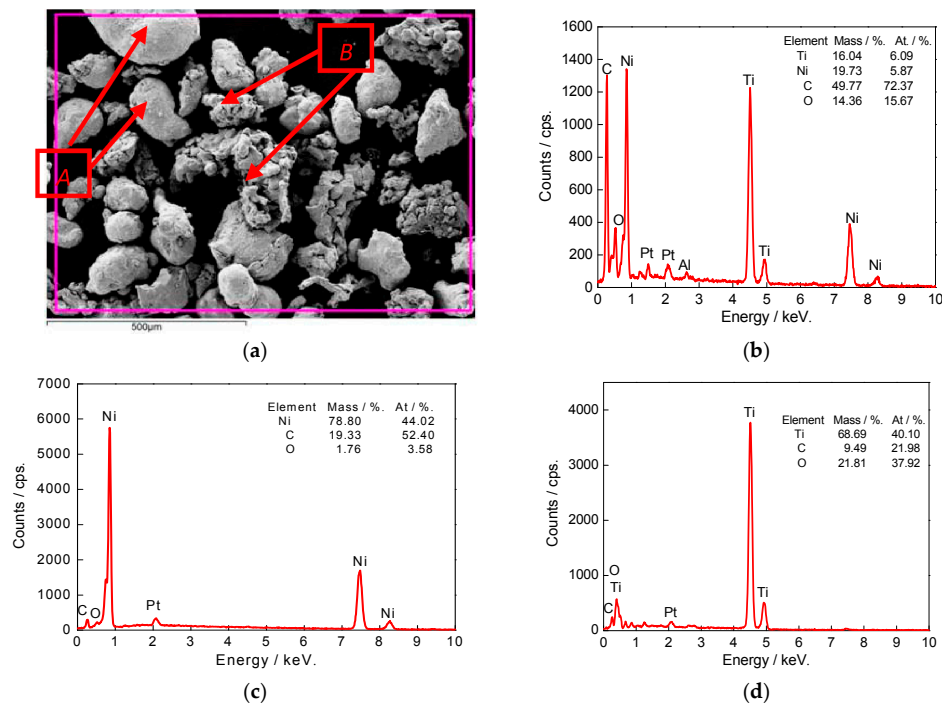


Figure 2. Morphologies and image mapping of Ti–Ni powders and EDS analysis of Ni and Ti particles. (a) Morphology of Ti–Ni powder; (b) Image mapping result of Ti–Ni powders; (c) EDS analysis result of Ni particle; and (d) EDS analysis result of Ti particle.

3.2. Image Mapping of Al–Ti–Ni Coating Surface

The image mapped position of the Al–Ti–Ni coating surface at the LR power of 600 W is shown in Figure 3a. Some small spherical un-melted particles, micro-cracks, and pores were present on the Al–Ti–Ni coating surface. This can be explained as follows: because the LR input power was too low, the arc-sprayed Al–Ti–Ni coating did not remelt fully; as a consequence, it became teardrop-shaped under the influence of surface tension force during the cooling period, and this resulted in the formation of small spherical unmelted particles. During the rapid crystallization phase, the growth of Al–Ti–Ni coating occurred in two directions, wherein the grains grew to collide with each other. At the same time, a microstress was produced at its bonding interface, and some microstructural defects such as grain boundary dislocations and vacancies were formed; this caused an increase in the defects in the solidified structure, an increase in the thermal brittleness, and a simultaneous decrease in the ductility and toughness. These defects ultimately became the source of microcracks. The existence of the molten pool was short with low laser power, causing the impurity components to not have enough time to float. In addition, the short duration of the molten pool also accelerated the cooling rate and increased the local temperature gradient, which enhanced local thermal stress, enlarged the cracking tendency and then produced the inclusion cracks. In addition, the presence of pores was attributed to the volume contraction of molten particles and the accumulation of gases in the molten particles when the Al–Ti–Ni coating was cooled to room temperature. Figure 3b shows the image mapping result of the Al–Ti–Ni coating surface at the LR power of 600 W. The Fe present in the Al–Ti–Ni coating was the result of Fe diffusion in the substrate, the C present in the Al–Ti–Ni coating was attributed to the air pollution, and the O present in the Al–Ti–Ni coating was attributed to the oxidation reaction that occurred during LR. The EDS analysis result shows that the Al peak was the strongest, indicating that the Al–Ti–Ni coating was composed mainly of Al. An Al-atom-rich zone was formed owing to the low LR power, which resulted in an insufficient overlap of Al–Ti–Ni coating, as shown in Figure 3c. The distribution of Ti was the same as that Al, as shown in Figure 3d. The Ni was uniformly distributed on Al–Ti–Ni coating surface, as shown in Figure 3e.

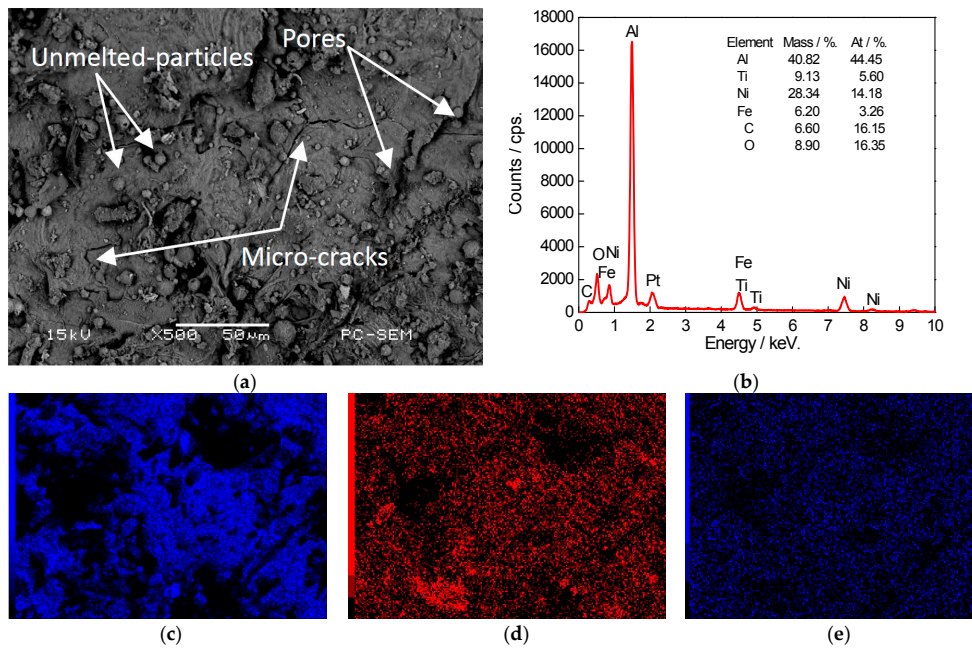


Figure 3. Image mapping analysis of Al–Ti–Ni coating at laser remelting (LR) power of 600 W. (a) Image mapped position; (b) Image mapping result; (c) Al content; (d) Ti content; and (e) Ni content.

The image mapped position of Al–Ti–Ni coating surface at the LR power of 800 W is shown in Figure 4a. Obvious pits, pores, and cracks were present on the coating surface. Although argon was used to protect the Al–Ti–Ni coating during LR, the coating surface was still partially oxidized at high temperature. During the LR test, pits were formed because of rapid cooling of Al–Ti–Ni coating whereas the pores were formed because the gas entered into the molten pool and the condensation speed was so fast that the gas could not be discharged in time and consequently remained in the condensed molten pool. In addition, because of fast heating and cooling speeds, the molten pool existed for a very short time, and so the oxides, sulfides and other impurities that were present in the molten pool were not released; this resulted in the formation of microcracks on the Al–Ti–Ni coating surface. Figure 4b shows the image mapping result of Al–Ti–Ni coating surface at the LR power of 800 W. It can be seen that the Al–Ti–Ni coating was composed primarily of Al, Ti, and Ni, and the C, Cl, Ca, and O were the impurities. The Al content was highest in the entire coating except in the pits, and this resulted in the formation of Al-atom-rich zones, as shown in Figure 4c. The Ti and Ni were well distributed and did not form atom-rich zones, as shown in Figure 4d,e.

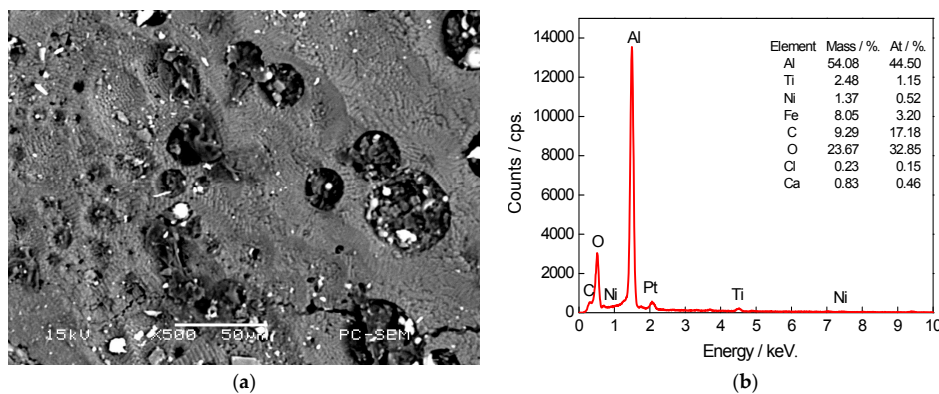


Figure 4. Cont.

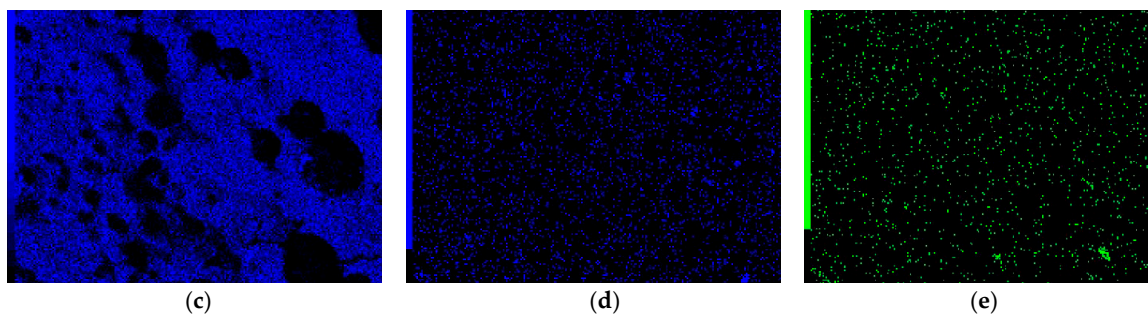


Figure 4. Image mapping analysis of Al-Ti-Ni coating at LR power of 800 W. (a) Image mapped position; (b) Image mapping result; (c) Al content; (d) Ti content; and (e) Ni content.

The image mapped position of the Al-Ti-Ni coating surface at the LR power of 1000 W is shown in Figure 5a. The coating surface was composed of ultrafine cellular structures of dissimilar sizes. The size of the cellular structure was related to the cooling rate. During the LR process, the grain diameter increased with increasing laser input energy and the self-cooling rate of grains decreased [31]. Therefore, the time taken for grain growth differed according to the self-cooling rates of grains [17]. This was because the remelting time of the Al-Ti-Ni coating in the molten pool increased with increasing LR powers, and the convective mass transfer occurred in the molten pool. The impurities in the molten liquid had sufficient time to float, which reduced the formation of inclusions and cracks in the Al-Ti-Ni coating and consequently improved its microstructure. Figure 5b shows the image mapping result of Al-Ti-Ni coating at the LR power of 1000 W. In this case, the Al-Ti-Ni coating was composed mainly of Al, Ti, and Ni, and the C, K, and Ca were the impurities. The EDS analysis shows that the mass fractions of Al and O accounted for 70.92% of total composition, indicating that the Al-Ti-Ni coating at the LR power of 1000 W was composed mainly of Al and O atoms. The Al, Ti, and Ni were evenly distributed, and no atom-rich zones were formed, as shown in Figure 5c–e.

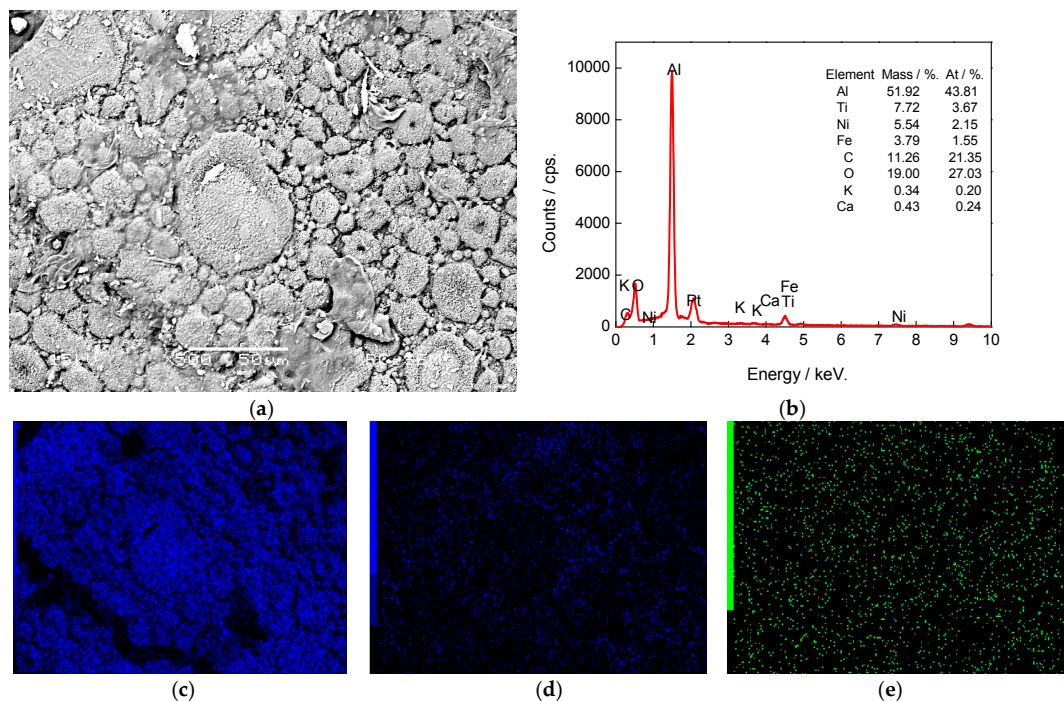


Figure 5. Image mapping analysis of Al-Ti-Ni coating at LR power of 1000 W. (a) Image mapped position; (b) Image mapping result; (c) Al content; (d) Ti content; and (e) Ni content.

3.3. Cross-Section Analysis of Al–Ti–Ni Coating between the Coating and the Substrate

The morphology of the Al–Ti–Ni coating cross-section at the LR power of 600 W is shown in Figure 6a. The Al–Ti–Ni coating was bonded with the substrate in a zigzag form. The presence of pores was due to the keyhole consisting of a slender vapor cavity present in the interaction region between the laser beam and the substrate. The keyhole was formed due to the vaporization of Al–Ti–Ni alloy. The instable keyhole led to a break in the capillarity, causing the formation of bubbles in the keyhole root. Due to the presence of an eddy flux, forward and downward, around the keyhole interface, the formed bubbles did not escape from the molten pool, but remained entrapped, therefore generating porosity at the end of the solidification process [32]. The Al formed obvious atom-rich zones, exhibiting irregular diffusion from the Al–Ti–Ni coating into the substrate, as shown in Figure 6b. The Ti content was higher, and the obvious diffusion of Ti also occurred at the interface; a small amount of Ti was present in the substrate, indicating that the Ti was diffused from the Al–Ti–Ni coating into the substrate. The diffusion degree of Ti was obviously higher than that of Al, as shown in Figure 6c. The Ni was uniformly distributed in the Al–Ti–Ni coating, and an obvious bright band was observed at the interface, which corresponded to the formed atom-rich zones, as shown in Figure 6d.

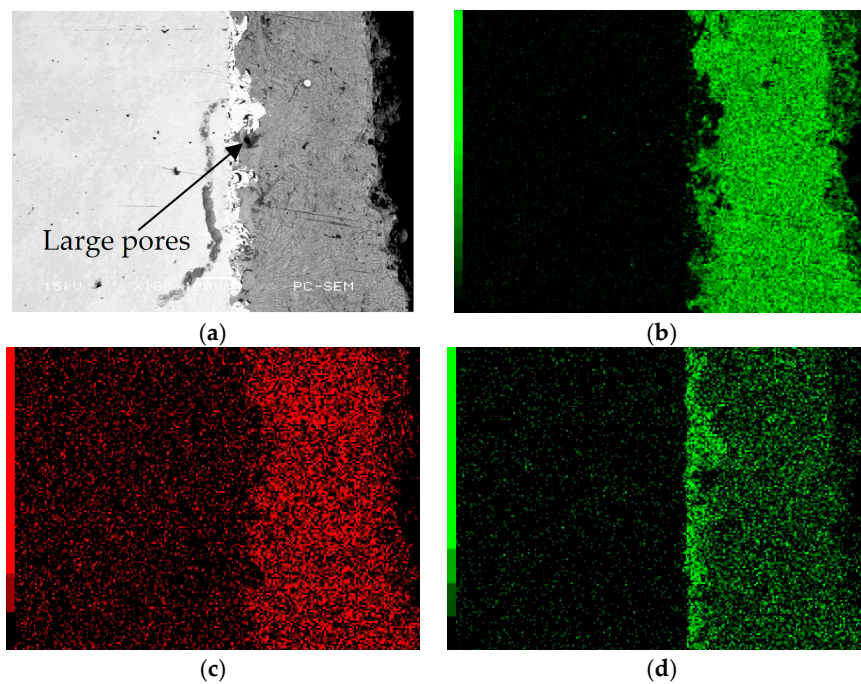


Figure 6. Image mapping analysis of Al–Ti–Ni coating cross section at LR power of 600 W. (a) Cross-sectional morphology; (b) Al content; (c) Ti content; and (d) Ni content.

The morphology of Al–Ti–Ni coating cross section at the LR power of 800 W is shown in Figure 7a. The formation of pores and pits was visualized more frequently than that of Al–Ti–Ni coating at the LR power of 600 W. At the LR power of 800 W, Al was evenly distributed over the Al–Ti–Ni coating cross section, indicating that the diffusion of Al–Ti–Ni coating at the LR power of 800 W was more regular than that at the LR power of 600 W, as shown in Figure 7b. The Ti shows the pronounced diffusion into the substrate, as can be seen in Figure 7c. The Ni was also diffused into the substrate, its diffusion shape was similar to that of Al, as shown in Figure 7d.

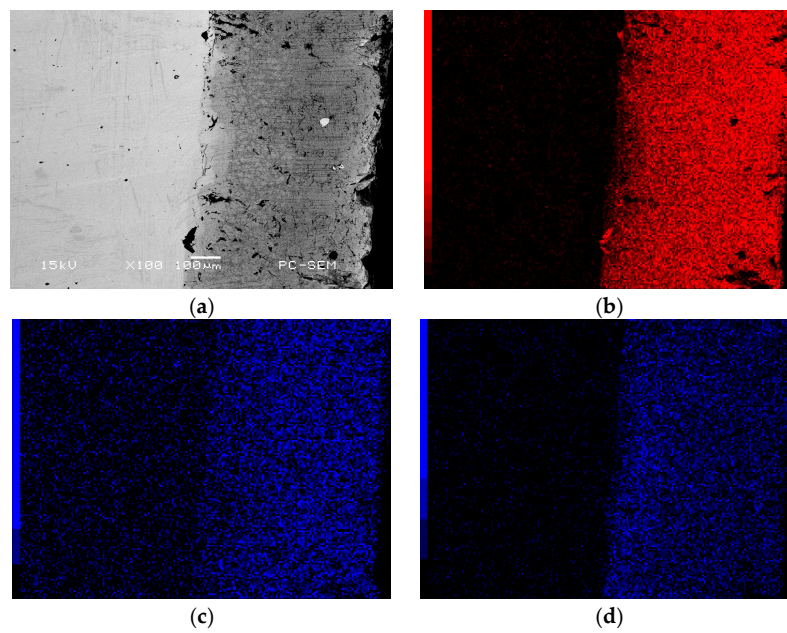


Figure 7. Image mapping analysis of Al–Ti–Ni coating cross-section at LR power of 800 W. (a) Cross-sectional morphology; (b) Al content; (c) Ti content; and (d) Ni content.

The morphology of Al–Ti–Ni coating cross-section at the LR power of 1000 W is shown in Figure 8a. The cross-section was uneven and a high fraction of pits were observed. At the LR power of 1000 W, the Al was uniformly distributed over the Al–Ti–Ni coating cross-section; its diffusion degree at this power was the smallest among those at the three considered powers, as shown in Figure 8b. The diffusion of Ti from the Al–Ti–Ni coating interface at the LR power of 1000 W was more obvious than that at the LR powers of 600 and 800 W, as shown in Figure 8c. At the LR power of 1000 W, the Ni was uniformly distributed over the Al–Ti–Ni coating cross-section and it was diffused into the substrate at the same time, as shown in Figure 8d.

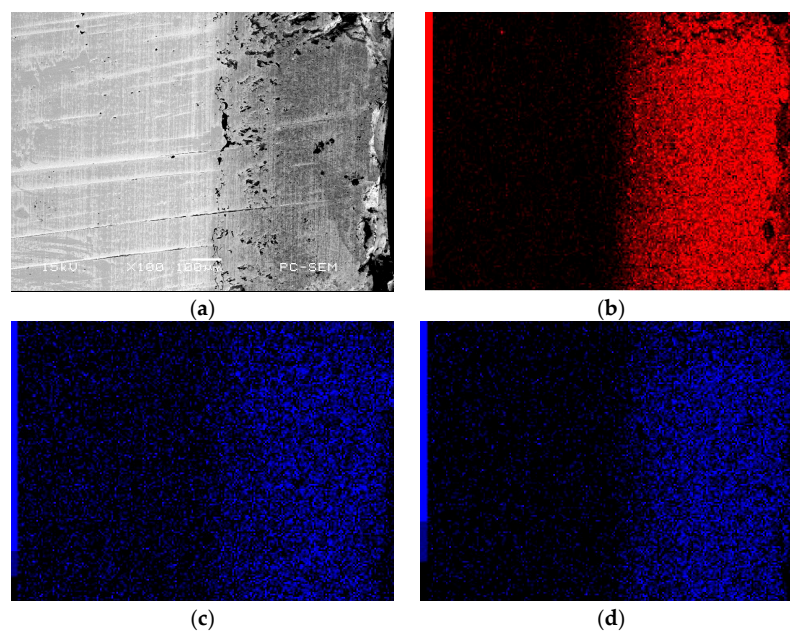


Figure 8. Image mapping analysis of Al–Ti–Ni coating cross-section at LR power of 1000 W. (a) Cross-sectional morphology; (b) Al content; (c) Ti content; and (d) Ni content.

3.4. Line Scan Analysis of Al–Ti–Ni Coating Cross-Section

The results of line scan analysis of Al–Ti–Ni coating cross-section at the LR power of 600 W are shown in Figure 9. The Al content of Al–Ti–Ni coating was very high and tended to stabilize, as shown in Figure 9a. The Ti content was maintained at a lower value in the substrate; it increased rapidly in the diffusion layer and remained at a certain value in the Al–Ti–Ni coating, as shown in Figure 9b. The Ni content of Al–Ti–Ni coating was higher; it decreased sharply from the Al–Ti–Ni coating to the substrate, and falling to a very low value in the substrate, as shown in Figure 9c.

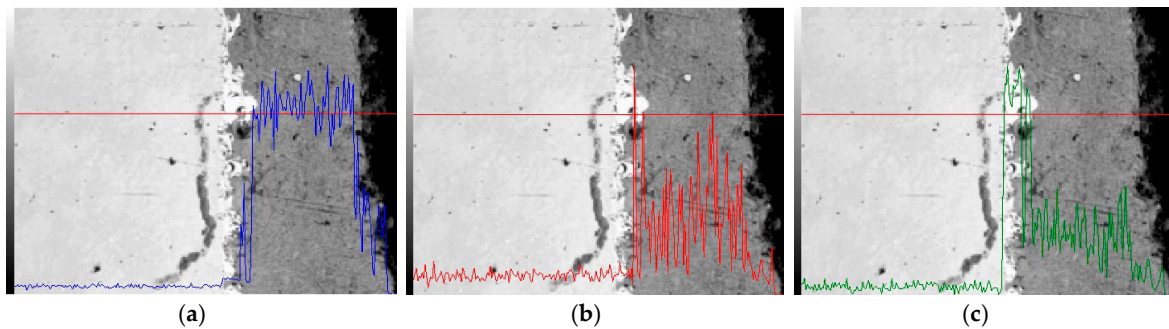


Figure 9. Line scan analysis of Al–Ti–Ni coating cross-section at LR power of 600 W. (a) Al content; (b) Ti content; and (c) Ni content.

The Al content of the substrate at the LR power of 800 W was almost 0, revealing a gradient trend in the coating, as shown in Figure 10a. The Ti content of substrate remained lower, rising in the small gradient in the diffusion layer, as shown in Figure 10b. The Ni content of substrate remained very low and increased sharply in the diffusion layer, as shown in Figure 10c.

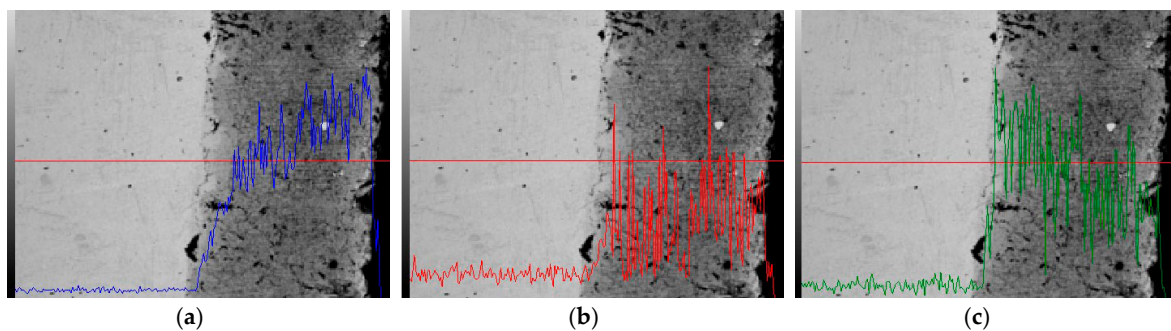


Figure 10. Line scan analysis of Al–Ti–Ni coating cross-section at LR power of 800 W. (a) Al content; (b) Ti content; and (c) Ni content.

The increment of Al content at the laser power of 1000 W was more obvious than that at the other two laser powers, and at 1000 W, the Al content of Al–Ti–Ni coating remained higher, as shown in Figure 11a. The Ti content of substrate remained at a low and stable value and increased sharply in the diffusion layer, as shown in Figure 11b. The Ni contents of Al–Ti–Ni coating and substrate generally remained lower, as shown in Figure 11c.

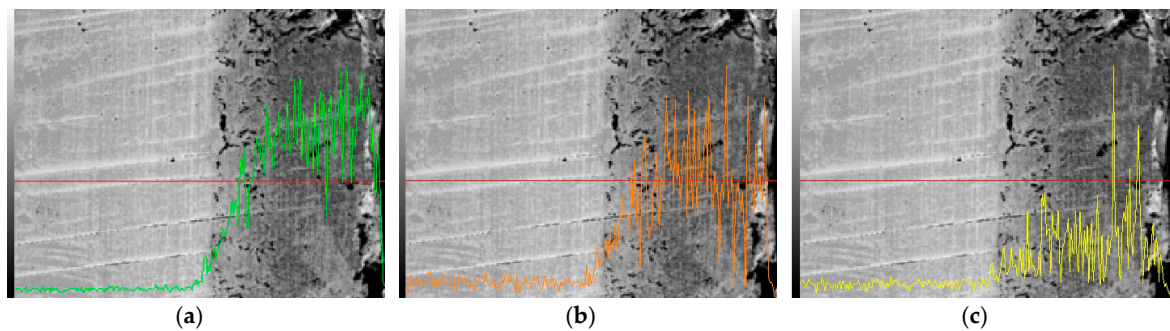


Figure 11. Line scan analysis of Al-Ti-Ni coating cross-section at LR power of 1000 W. (a) Al content; (b) Ti content; and (c) Ni content.

From the above analyses, it can be seen that the Al, Ti, and Ni atoms at the interface were diffused into the substrate and formed metallurgical bonding, thereby improving the bonding strength of Al-Ti-Ni coating.

3.5. XRD Analysis

The XRD analysis of Al-Ti-Ni coating at the LR power of 600 W mainly revealed the presence of intermetallic compound phases related to Al-Ti and Al-Ni; the diffraction peaks of Al_3Ti , Al_3Ni , and Al_3Ni_2 phases were detected at 39.021° , 45.059° , and 79.5° – 86° , respectively. The broadened diffraction peaks and low diffraction intensity indicated that the degree of crystallinity was not high and the amorphous phase was formed, as shown in Figure 12a.

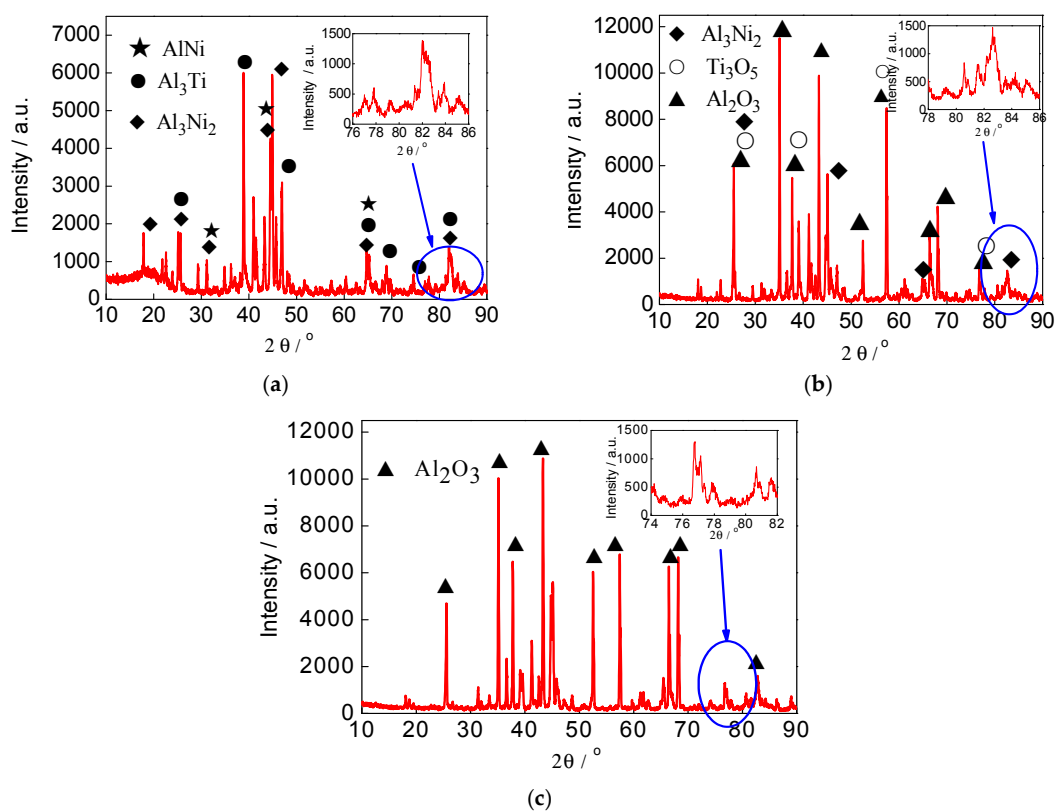


Figure 12. XRD spectra of Al-Ti-Ni coatings at different LR powers (a) LR power of 600 W; (b) LR power of 800 W; and (c) LR power of 1000 W.

At the LR power of 800 W, the Al_3Ni_2 , Al_2O_3 , and Ti_3O_5 phases were detected in the Al–Ti–Ni coating at 25.520° and the Al_2O_3 phase was detected at 35.063° , indicating that the interior of the Al–Ti–Ni coating was crystallized. The Al_2O_3 and Ti_3O_5 phases were detected at 57.399° , indicating that the Al and Ti were reacted with the O to induce the mixed oxidations during the LR test. A low-intensity diffraction peak was detected at $78^\circ\text{--}86^\circ$, indicating that the amorphous phase existed; it was detected mainly in the form of Al_3Ni_2 , Al_2O_3 , and Ti_3O_5 , as shown in Figure 12b.

At the LR power of 1000 W, a strong diffraction peak of Al_2O_3 in the Al–Ti–Ni coating was detected at 43.302° and some Al_2O_3 sub-peaks were also detected; no other intermetallic phase was detected. The amorphous Al_2O_3 phase was detected at $75^\circ\text{--}82^\circ$, as shown in Figure 12c. The laser-remelted Al–Ti–Ni coating was composed primarily of Al oxide. However, the intermetallic phase disappeared with an increase in the LR power; this was because a sufficient time and temperature were required for the formation of intermetallic compounds [33,34], and the remelting time decreased the compound formation with the LR powers increasing.

3.6. Scanning Analysis of Corrosion Products

Figure 13a shows the image mapped position of Al–Ti–Ni coating at the LR power of 600 W. In this case, the Al–Ti–Ni coating surface was coarse and the corrosion was uneven. Exfoliation corrosion and corrosion pits of different sizes were observed on the coating surface, and the main mechanism of corrosion was pitting corrosion. The corrosion occurred at the sites of pores and cracks, resulting in localized corrosion and the formation of numerous white corrosion products on the pit surface. Figure 13b shows the image mapping result of Al–Ti–Ni coating at the LR power of 600 W after immersion corrosion; it can be seen that the mass fractions of Al, Ti, and Ni on the Al–Ti–Ni coating surface accounted for 69.38% of the total composition. Al was evenly distributed on the coating surface, except at the sites of the pits, and the Al-atom-rich zones were formed, as shown in Figure 13c. The Ti and Ni were evenly distributed and no atom-rich zones were formed, as shown in Figure 13d,e.

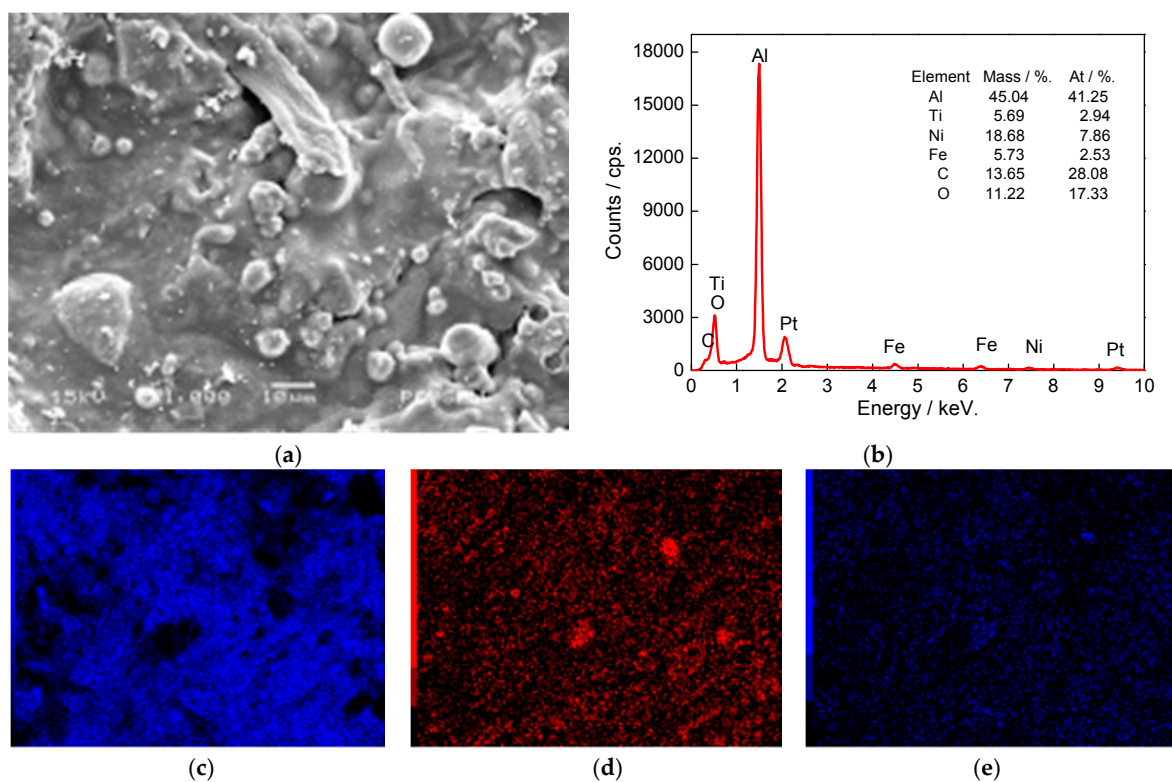


Figure 13. Image mapping analysis of Al–Ti–Ni coating at LR power of 600 W after immersion corrosion (a) Image mapped position; (b) Image mapping result; (c) Al content; (d) Ti content; and (e) Ni content.

Figure 14a shows the image mapped position of Al–Ti–Ni coating at the LR power of 800 W. The corrosion surface was uneven and massive corrosion holes and pits were present on the Al–Ti–Ni coating surface. The corrosion products were mainly stacked on the Al–Ti–Ni coating surface. Figure 14b shows the image mapping result of Al–Ti–Ni coating at the LR power of 800 W after immersion corrosion; in this case, the mass fractions of Al, Ni, and O accounted for 71.57% of total composition. The Al, Ti, and Ni appeared the defects on the atom-poor zones, as shown in Figure 14c–e.

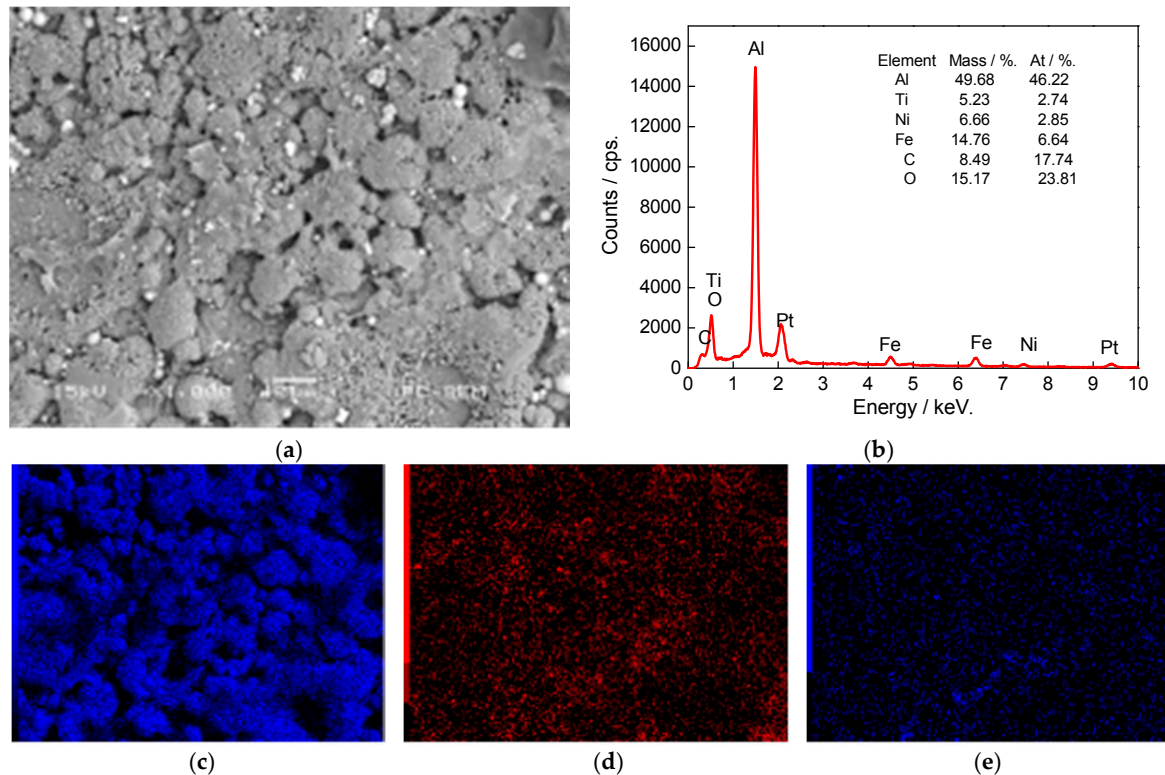


Figure 14. Image mapping analysis of Al–Ti–Ni coating at LR power of 800 W after immersion corrosion (a) Image mapped position; (b) Image mapping result; (c) Al content; (d) Ti content; and (e) Ni content.

Figure 15a shows the image mapped position of Al–Ti–Ni coating at the LR power of 1000 W. The Al–Ti–Ni coating surface was smooth, and no large corrosion pits were observed. The corrosion mechanism was uniform corrosion. Unlike in the case of the Al–Ti–Ni coatings at the LR powers of 600 and 800 W, at the LR power of 1000 W, the corrosion products were formed on the Al–Ti–Ni coating surface, thereby reducing the degree of corrosion; this demonstrated the excellent corrosion resistance of Al–Ti–Ni coating at this LR power. The Al and O on the Al–Ti–Ni coating surface accounted for 79.2% of the total composition, as shown in Figure 15b. This indicated that the corrosion products were mainly the oxides of Al and O, which provided an effective corrosion protection barrier in the immersion corrosion test. The Al, Ti, and Ni were evenly distributed, and no atom-rich zones were formed, as shown in Figure 15c–e.

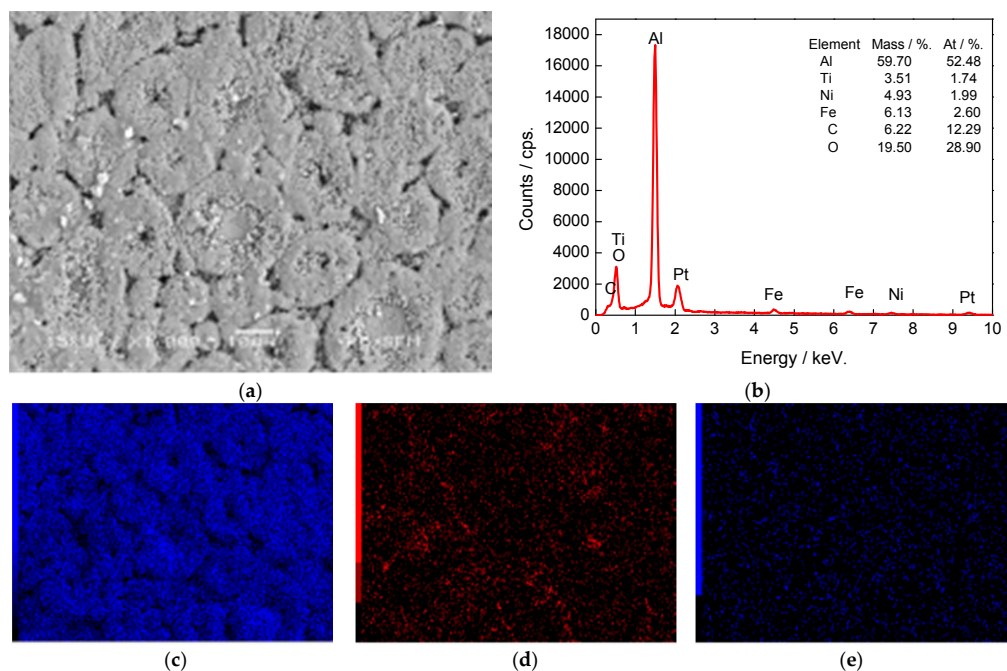


Figure 15. Image mapping analysis of Al–Ti–Ni coating at LR power of 1000 W after immersion corrosion (a) Image mapped position; (b) Image mapping result; (c) Al content; (d) Ti content; and (e) Ni content.

From the above analyses, it can be seen that the LR power had a significant influence on the immersion corrosion of Al–Ti–Ni coating. At the LR power of 600 W, the Al–Ti–Ni coating did not melt completely and many surface defects were formed, as a result of which it could not protect the substrate effectively. In contrast, at the LR power of 1000 W, the Al–Ti–Ni coating formed a uniform and dense passive film, and no pores and cracks were formed. The corrosion resistance of Al–Ti–Ni coating improved effectively, indicating that the corrosion resistance of the coating subjected to LR treatment increased with increasing LR power.

3.7. Corrosion Mechanism

Figure 16a shows the corrosion morphology of Al–Ti–Ni coating at the LR power of 600 W. The Al–Ti–Ni coating surface was rough and many microcracks were present, indicating the occurrence of severe corrosion damage. A rough surface could induce severe pitting corrosion [25]. The poor corrosion resistance in this case was attributed to the presence of cracks and pores shown in Figure 3a. The active Cl^- anions in the medium were first adsorbed on these defects, after which they acquired enough mobility to diffuse through the cracks and pores preferentially [35]. This accelerated the damage of Al–Ti–Ni coating surface, which, in turn, promoted the formation of corrosion pits by local corrosion of the pits' surfaces and caused pitting and localized corrosion.

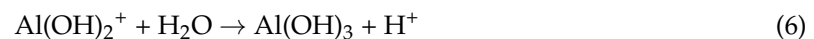
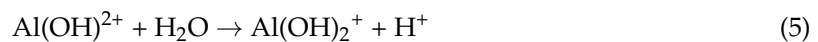
The white corrosion products were round in shape and attached to the Al–Ti–Ni coating surface, thereby covering the pit orifice. Figure 16b shows the corrosion morphology of Al–Ti–Ni coating at the LR power of 800 W. The corrosion surface showed a regular distribution of the round products, indicating the existence of corrosion pits; considerable local corrosion was found to occur. The pitting corrosion is a localized form of attack that results in relatively rapid penetration in small discrete areas. One of the major reasons for pitting was fragility of passive film, which led to its breakdown [36]. Because the oxide film on the coating surface was thin, the aggressive ions such as Cl^- , which were present on the coating surface, were crucial to the breakdown of the passive film, and this consequently initiated the localized corrosion. Therefore, the coating corrosion resistance was greatly reduced at this power.

Figure 16c shows the corrosion morphology of Al–Ti–Ni coating at the LR power of 1000 W. The Al–Ti–Ni coating surface was relatively smooth and partial pitting was observed. After immersion corrosion, a compact protective Al film was formed, and slight but uniform corrosion occurred; the corrosion products were scattered on the Al–Ti–Ni coating surface. This was mainly due to the redistribution of laser-remelted Al on the Al–Ti–Ni coating, which resulted in the formation of Al-atom-rich zones and the protective oxide of Al₂O₃. On the one hand, it acted as a barrier to the corrosive medium, and on the other hand, it slowed down both the consumption of Al and the corrosion rate to a certain extent.

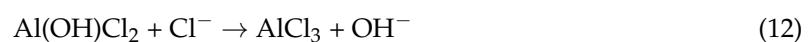
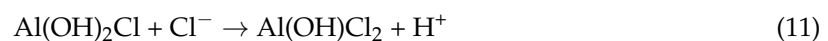
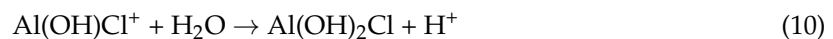
In 3.5% NaCl solution, the following chemical reactions occurred at the cathode:



The following chemical reactions occurred at the anode:



As can be seen in Reactions (4)–(6), although Al(OH)²⁺ was an intermediate product, it also reacted with the Cl[−]:



Therefore, a cathodic reaction in addition to Reaction (1) occurred, given as



The AlCl₃ formed in the reactions in Reactions (8)–(12) could easily be hydrolyzed in water; therefore, the Cl element in the corrosion products could not be detected.

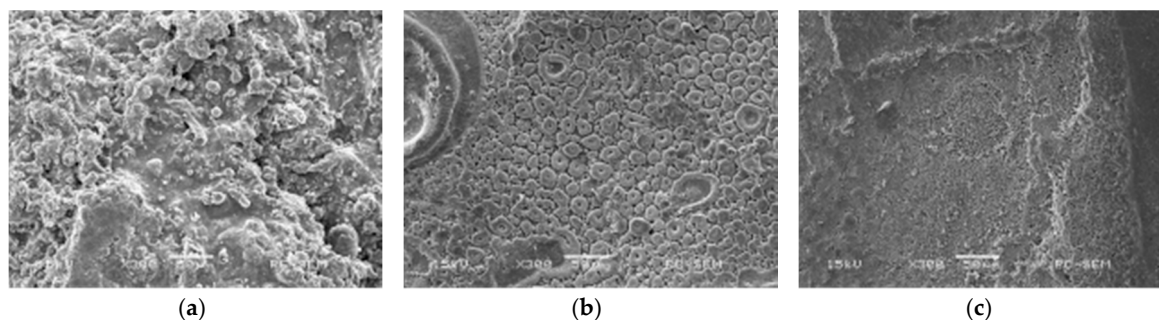


Figure 16. Corrosion morphologies of Al–Ti–Ni coatings at different LR powers. (a) LR power of 600 W; (b) LR power of 800 W; and (c) LR power of 1000 W.

At the LR power of 1000 W, the Al_3Ni phase of Al–Ti–Ni coating disappeared after immersion corrosion and a new phase—AlNi—was formed, as shown in Figure 17a. A comparison of this figure with Figure 12a reveals that the intensities of Al_3Ni_2 and Al_3Ti peaks decreased noticeably after immersion corrosion, indicating the consumption of Al_3Ni_2 and Al_3Ti phases and the formation of AlNi phase. At the LR power of 800 W, the formed Ti_3O_5 phase of Al–Ti–Ni coating disappeared, as shown in Figure 17b. This was due to the degradation of Ti_3O_5 passivation film during the immersion corrosion test. As the corrosion time increased, the Ti content was not sufficient to sustain the growth of Ti_3O_5 consumption; then, the Al was consumed, which resulted in the formation of an Al_2O_3 passivation film on the coating surface. This was also the reason why the protective properties of Al–Ti–Ni coating at the LR power of 800 W were not compromised after the immersion corrosion test. The corrosion of Al–Ti–Ni coating was more obvious at the LR power of 1000 W, and the peak of Al_2O_3 , which was produced during the immersion corrosion test, was also more obvious; the new Al_3Ni_2 phase was also formed, but its peak intensity was not high. The trend of peak broadening indicated the presence of amorphous phase, as shown in Figure 17c. Therefore, owing to the higher content of amorphous phase and fewer pores and cracks, the Al–Ti–Ni coating at the LR power of 1000 W was superior to those at the other two LR powers.

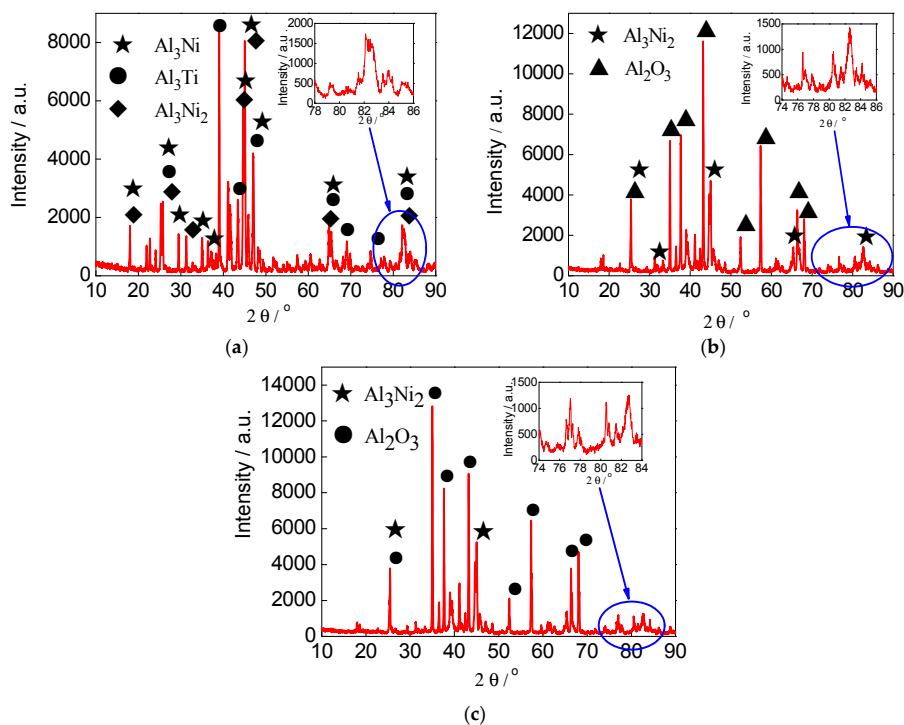


Figure 17. XRD analysis results of Al–Ti–Ni coatings at different LR powers after immersion corrosion (a) LR power of 600 W; (b) LR power of 800 W; and (c) LR power of 1000 W.

3.8. Electrochemical Corrosion

Figure 18 shows the potentiodynamic polarization curves of laser-remelted Al–Ti–Ni coatings in 3.5% NaCl solution. The important corrosion resistance parameters of Al–Ti–Ni coating were the corrosion potential (E_{corr}) and corrosion current density (i_{corr}). Generally, when the corrosion potentials shifted positively, the corrosion rates decreased and the corrosion resistance was enhanced [37]. The E_{corr} values of Al–Ti–Ni coating at the LR powers of 600, 800, and 1000 W were -0.586 , -0.399 , and -0.233 V, respectively, and the corresponding i_{corr} values were 10×10^{-7} , 10×10^{-10} , and 10×10^{-10} A/cm², respectively. The E_{corr} and i_{corr} values of substrate were -0.715 V and 10×10^{-8} A/cm², respectively. The E_{corr} values of Al–Ti–Ni coating at the LR powers of 600, 800, and 1000 W were higher than that of

substrate. This was because the forming intermetallic compounds of Ni, Ti and Al by XRD analysis all had anti-resistance than S355 steel [38]. The positive shift of E_{corr} shows that the electrochemical corrosion resistance of Al–Ti–Ni coating was superior to that of substrate. The Al–Ti–Ni coating at the LR power of 1000 W had the smallest corrosion potential and a smaller corrosion current density, demonstrating that its electrochemical corrosion resistance was the highest.

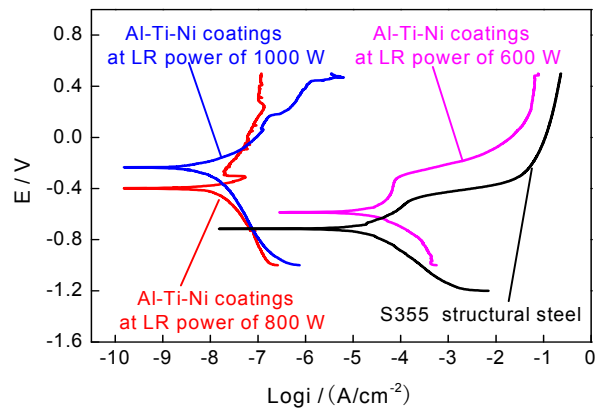


Figure 18. Polarization curves of Al–Ti–Ni coatings at different LR powers and substrate.

Its corrosion rate can be expressed as

$$V = \frac{Ai_{\text{corr}}}{nF} \quad (14)$$

where A was the atomic weight of the metal; i_{corr} was the current density; n was the number of the electron transfer; and F was the Faraday constant.

From Equation (14), it can be seen that the corrosion rate (V) was proportional to the electrode corrosion current density (i_{corr}); this suggested that the higher was the corrosion rate, the higher was the electrode corrosion current density. From the viewpoint of the corrosion rate, the electrode corrosion current density of Al–Ti–Ni coating at the LR power of 1000 W was close to that at the LR power of 800 W and much smaller than those of Al–Ti–Ni coating at the LR power of 600 W and substrate. The corrosion potential of the coating at the LR power of 1000 W shows a positive shift; its electrochemical corrosion resistance was superior to those of Al–Ti–Ni coatings at the other two LR powers. That is, the Al–Ti–Ni coating at the LR power of 1000 W shows the best corrosion resistance. From these analyses, it can be seen that the passive film formed on the surface of laser–remelted Al–Ti–Ni coating at the LR power of 1000 W was the main factor that contributed to the improvement in the electrochemical corrosion resistance of Al–Ti–Ni coatings.

4. Conclusions

- At the LR powers of 600, 800, and 1000 W, the Al–Ti–Ni coating forms a metallurgical bonding with the substrate; the Al–Ti–Ni coating at the LR power of 1000 W shows the best surface and cross-sectional qualities and best performance. Certain amounts of AlNi, Al₃Ti, Al₃Ni₂, Ti₃O₅, and Al₂O₃ amorphous phases are detected.
- The microstructure of Al–Ti–Ni coating at the LR power of 1000 W is uniform, and no obvious defects such as cracks and pores are observed. The corrosion mechanisms are pitting corrosion and uniform corrosion. In contrast, cracks and pores are present on the Al–Ti–Ni coating surfaces at the LR powers of 600 and 800 W, and the corrosion mechanisms are localized corrosion and pitting corrosion.
- Amorphous phases are detected in the Al–Ti–Ni coating at the LR powers of 600, 800, and 1000 W, and their corrosion potentials are higher than that of S355 steel; this indicates that the

laser-remelted Al–Ti–Ni coating improves the electrochemical corrosion resistance of S355 steel. The electrochemical corrosion resistance increases with increasing LR powers.

- The corrosion potentials of Al–Ti–Ni coatings at the LR powers of 600, 800, and 1000 W are -0.586 , -0.399 , and -0.233 V, respectively. The corrosion potential of Al–Ti–Ni coating at the LR power of 1000 W shows a positive shift, indicating its higher electrochemical corrosion resistance.

Acknowledgments: Financial support for this research by the Key Research and Development Project of Jiangsu Province (BE2016052) is gratefully acknowledged.

Author Contributions: Dejun Kong and Haixiang Chen conceived and designed the experiments; Haixiang Chen performed the experiments, analysed the data, and wrote the manuscript; Dejun Kong revised the manuscript and was the corresponding author.

Conflicts of Interest: The authors declare no conflict of interest.

References

1. Fernández, R.P.; Pardo, M.L. Offshore concrete structures. *Ocean Eng.* **2013**, *58*, 304–316. [[CrossRef](#)]
2. Choe, S.B.; Lee, S.J. Effect of flow rate on electrochemical characteristics of marine material under seawater environment. *Ocean Eng.* **2017**, *141*, 18–24. [[CrossRef](#)]
3. Kwon, S.J.; Lee, H.S.; Karthick, S.; Saraswathy, V.; Yan, H.M. Long-time corrosion performance of blended cement concrete in the marine environment—A real-time study. *Constr. Build. Mater.* **2017**, *154*, 349–360. [[CrossRef](#)]
4. Zhao, T.L.; Liu, Z.Y.; Du, C.W.; Dai, C.D.; Li, X.G.; Zhang, B.W. Corrosion fatigue crack initiation and initial propagation mechanism of E690 steel in simulated seawater. *Mater. Sci. Eng. A* **2017**, *708*, 181–192. [[CrossRef](#)]
5. Gao, W.B.; Wang, D.P.; Cheng, F.J.; Di, X.J.; Deng, C.Y.; Xu, W. Microstructural and mechanical performance of underwater wet welded S355 steel. *J. Mater. Process. Technol.* **2016**, *238*, 333–340. [[CrossRef](#)]
6. Liu, G.J.; Zhai, Y.Z.; Leng, D.X.; Tian, X.J.; Mu, W.L. Research on structural damage detection of offshore platforms based on grouping modal strain energy. *Ocean Eng.* **2017**, *140*, 43–49. [[CrossRef](#)]
7. Zeman, P.; Zitek, M.; Zuzjakova, S.; Cerstvy, R. Amorphous Zr-Cu thin-film alloys with metallic glass behavior. *J. Alloys Compd.* **2017**, *696*, 1298–1306. [[CrossRef](#)]
8. Tavoosi, M.; Barahimi, A. Corrosion behavior of amorphous–nanocrystalline Fe–Ni–Cr electrodeposited coatings. *Surf. Interfaces* **2017**, *8*, 103–111. [[CrossRef](#)]
9. Liu, J.T.; Hou, J.X.; Zhang, X.R.; Guo, J.; Xu, L.F.; Fan, G.J. Influence of remelting treatment on corrosion behavior of amorphous alloys. *Rare Met. Mater. Eng.* **2017**, *46*, 296–300.
10. Cheng, J.B.; Wang, B.L.; Liu, Q.; Liang, X.B. In-situ synthesis of novel Al–Fe–Si metallic glass coating by arc spraying. *J. Alloys Compd.* **2017**, *716*, 88–95. [[CrossRef](#)]
11. Tan, Z.; Xue, Y.F.; Cheng, X.W.; Zhang, L.; Chen, W.W.; Wang, L.; Zhang, H.F.; Fu, H.M. Effect of element fitting on composition optimization of Al–Cu–Ti amorphous alloy by mechanical alloying. *Trans. Nonferrous Met. Soc. China* **2015**, *25*, 3348–3353. [[CrossRef](#)]
12. Shen, Y.; Perepezko, J.H. Al-based amorphous alloys: Glass-forming ability, crystallization behavior and effects of minor alloying additions. *J. Alloys Compd.* **2017**, *707*, 3–11. [[CrossRef](#)]
13. Shakhova, I.; Mironov, E.; Azarmi, F.; Safonov, A. Thermo-electrical properties of the alumina coatings deposited by different thermal spraying technologies. *Ceram. Int.* **2017**, *43*, 15392–15401. [[CrossRef](#)]
14. Zhou, J.X.; Yang, M.C.; Wang, R.Q.; Pang, X.M. Annealing behavior of aluminum coating prepared by arc spraying on P355NL1 steel. *Surf. Coat. Technol.* **2017**, *330*, 53–60. [[CrossRef](#)]
15. Hazra, S.; Das, J.; Bandyopadhyay, P.P. Synthesis of mullite-based coatings from alumina and zircon powder mixtures by plasma spraying and laser remelting. *Mater. Chem. Phys.* **2015**, *154*, 22–29. [[CrossRef](#)]
16. Park, I.C.; Kim, S.J. Corrosion behavior in seawater of arc thermal sprayed Inconel 625 coatings with sealing treatment. *Surf. Coat. Technol.* **2017**, *325*, 729–737. [[CrossRef](#)]
17. Wang, D.S.; Tian, Z.J.; Shen, L.D.; Liu, Z.D.; Huang, Y.H. Influences of laser remelting on microstructure of nanostructured Al₂O₃-13 wt.% TiO₂ coatings fabricated by plasma spraying. *Appl. Surf. Sci.* **2009**, *255*, 4606–4610. [[CrossRef](#)]
18. Lin, X.; Cao, Y.Q.; Wang, Z.T.; Cao, J.; Wang, L.L.; Huang, W.D. Regular eutectic and anomalous eutectic growth behavior in laser remelting of Ni-30 wt.% Sn alloys. *Acta Mater.* **2017**, *126*, 210–220. [[CrossRef](#)]

19. Zhang, P.L.; Yan, H.; Yao, C.W.; Li, Z.G.; Yu, Z.S.; Xu, P.Q. Synthesis of Fe–Ni–B–Si–Nb amorphous and crystalline composite coatings by laser cladding and remelting. *Surf. Coat. Technol.* **2011**, *206*, 1229–1236. [[CrossRef](#)]
20. Wang, L.; Yao, J.H.; Hu, Y.; Song, S.Y. Suppression effect of a steady magnetic field on molten pool during laser remelting. *Appl. Surf. Sci.* **2015**, *351*, 794–802. [[CrossRef](#)]
21. Li, C.G.; Yu, Z.S.; Zhang, Y.F.; Zhang, P.L.; Yan, H.; Lu, Q.H.; Li, W.G.; Wang, Y. Microstructure evolution of laser remelted Al₂O₃–13 wt.% TiO₂ coatings. *J. Alloys Compd.* **2013**, *576*, 187–194. [[CrossRef](#)]
22. Yu, J.B.; Wang, Y.; Zhou, F.F.; Wang, L.; Pan, Z.Y. Laser remelting of plasma-sprayed nanostructured Al₂O₃–20 wt.% ZrO₂ coatings onto 316L stainless steel. *Appl. Surf. Sci.* **2017**. [[CrossRef](#)]
23. Zhang, J.F.; Liu, M.; Song, J.B.; Deng, C.M.; Deng, C.G. Microstructure and corrosion behavior of Fe-based amorphous coating prepared by HVOF. *J. Alloys Compd.* **2017**, *721*, 506–511. [[CrossRef](#)]
24. Li, Q.; Liu, S.S.S.; Wang, X.H.; Yang, T.; Dong, C.; Hu, J.T.; Jiang, Y.Q. Mechanical and corrosion properties of Ti–Ni–Cu–Zr metallic glass matrix composites. *J. Alloys Compd.* **2017**, *727*, 1344–1350. [[CrossRef](#)]
25. Zhao, Y.T.; Jiang, C.H.; Xu, Z.; Cai, F.; Zhang, Z.Q.; Fu, P. Microstructure and corrosion behavior of Ti nanoparticles reinforced Ni–Ti composite coatings by electrodeposition. *Mater. Des.* **2015**, *85*, 39–46. [[CrossRef](#)]
26. Tan, C.L.; Zhu, H.M.; Kuang, T.C.; Shi, J.; Liu, H.W.; Liu, Z.W. Laser cladding Al-based amorphous–nanocrystalline composite coatings on AZ80 magnesium alloy under water cooling condition. *J. Alloys Compd.* **2017**, *690*, 108–115. [[CrossRef](#)]
27. Wang, Q.Y.; Xi, Y.C.; Zhao, Y.H.; Liu, S.; Bai, S.L.; Liu, Z.D. Effects of laser re-melting and annealing on microstructure, mechanical property and corrosion resistance of Fe-based amorphous/crystalline composite coating. *Mater. Charact.* **2017**, *127*, 239–247. [[CrossRef](#)]
28. Li, R.F.; Jin, Y.J.; Li, Z.G.; Zhu, Y.Y.; Wu, M.F. Effect of the remelting scanning speed on the amorphous forming ability of Ni-based alloy using laser cladding plus a laser remelting process. *Surf. Coat. Technol.* **2014**, *259*, 725–731. [[CrossRef](#)]
29. Wang, S.L.; Zhang, Z.Y.; Gong, Y.B.; Nie, G.M. Microstructures and corrosion resistance of Fe-based amorphous/nanocrystalline coating fabricated by laser cladding. *J. Alloys Compd.* **2017**, *728*, 1116–1123. [[CrossRef](#)]
30. *GB/T 6458-86 Metallic Coatings—Neutral Salt Spray Test (Nss Test)*; Standards Administration of China: Beijing, China, 1986.
31. Cong, D.L.; Li, Z.S.; He, Q.B.; Chen, D.J.; Chen, H.B.; Yang, J.Z.; Zhang, P.; Zhou, H. Effects of unit size on thermal fatigue behavior of hot work steel repaired by a biomimetic laser remelting process. *Opt. Laser Technol.* **2018**, *98*, 205–213. [[CrossRef](#)]
32. Da Silva, M.R.; Gargarella, P.; Gustmann, T.; Botta Filho, W.J.; Kiminami, C.S.; Eckert, J.; Pauly, S.; Bolfarini, C. Laser surface remelting of a Cu–Al–Ni–Mn shape memory alloy. *Mater. Sci. Eng. A* **2016**, *661*, 61–67. [[CrossRef](#)]
33. Sichani, H.R.; Salehi, M.; Edris, H.; Farani, M.T. The effect of APS parameter on the microstructural, mechanical and corrosion properties of plasma sprayed Ni–Ti–Al intermetallic coatings. *Surf. Coat. Technol.* **2017**, *309*, 959–968. [[CrossRef](#)]
34. Li, K.; Li, Y.; Huang, X.; Gibson, D.; Zheng, Y.; Liu, J.; Sun, L.; Fu, Y.Q. Surface microstructures and corrosion resistance of Ni–Ti–Nb shape memory thin films. *Appl. Surf. Sci.* **2017**, *414*, 63–67. [[CrossRef](#)]
35. Fan, Z.J.; Wang, K.D.; Dong, X.; Duan, W.Q.; Wang, R.J.; Mei, X.S.; Wang, W.J.; Cui, J.L.; Zhang, S.; Xu, C.H. Evaluation of microstructural evolution and corrosion types in ultrasonic assisted laser re-melted thermal barrier coatings under exposure to molten salts. *Mater. Lett.* **2017**, *188*, 145–148. [[CrossRef](#)]
36. Sun, Z.; Annergren, I.; Pan, D.; Mai, T.A. Effect of laser surface remelting on the corrosion behavior of commercially pure titanium sheet. *Mater. Sci. Eng. A* **2003**, *345*, 293–300. [[CrossRef](#)]
37. Zhang, X.; Mi, G.Y.; Xiong, L.D.; Wang, C.M. Effects of interlaminar microstructural inhomogeneity on mechanical properties and corrosion resistance of multi-layer fiber laser welded high strength low alloy steel. *J. Mater. Process. Technol.* **2018**, *252*, 81–89. [[CrossRef](#)]
38. Liu, F.C.; Mao, Y.Q.; Lin, X.; Zhou, B.S.; Qian, T. Microstructure and high temperature oxidation resistance of Ti–Ni gradient coating on TA2 titanium alloy fabricated by laser cladding. *Opt. Laser Technol.* **2016**, *83*, 140–147. [[CrossRef](#)]

